Sedimentation, Orientation and Dispersal of Ramified Particles in a Turbulent Environment
W911NF-15-1-0205

Donald L. Koch, Cornell University, and Greg Voth, Wesleyan University

Understanding the behavior of suspended particles in turbulent flows is among the most important fundamental challenges in fluid mechanics. Most previous studies have considered particles that are either spherical, have a small particle Reynolds number, or (in most cases) both. This project provides the first experimental measurements and theoretical predictions for the orientation, sedimentation rate and dispersive behavior of non-spherical finite Reynolds number particles in homogeneous isotropic turbulence. The study focuses on ramified particles consisting of interconnected rods because of the advantages of these particles for flow visualization experiments and asymptotic theory (slender-body theory).

When non-spherical particles with a finite particle Reynolds number settle in a quiescent fluid they experience a torque due to inertial effects associated with
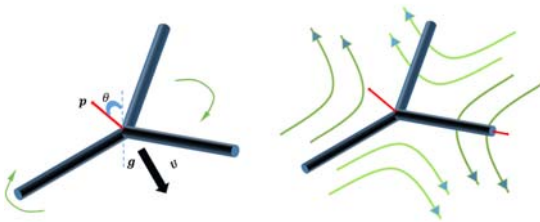

Figure 1 Triad particle experiencing the competing effects of an inertial torque due to settling which favors broadside orientations (right) and rotation due to turbulent shearing motion that randomizes orientation (left).

their fluid velocity disturbance that rotates the particles toward a broadside orientation (Figure 1). In an isotropic turbulent flow, the temporally fluctuating turbulent velocity rotates particles and tends to randomize their orientation. Section 1 of this report describes a model for the orientation of slender fibers that incorporates the first effect of the inertial torque for small, but non-zero particle Reynolds number based on the particle length and predicts the dependence of the particle orientation on turbulence intensity. Section 2 extends this model to describe the orientation of planar, triad particles settling in isotropic turbulence. In section 3, we present experimental observations of particle orientation, settling velocity and dispersive motion for a range of particle sizes and turbulence intensities and interpret these measurements in terms of the model. Section 4 presents experimental measurements and theoretical calculations for the motion of both symmetric and asymmetric fibers settling in a quiescent fluid. This study allowed us to validate the inertial slender-body theory predictions that underlie our treatment of particles in turbulent flows. In addition, we discovered a transition from vertical to oblique alignment of asymmetric particles at a critical Reynolds number or degree of asymmetry. Section 5 reports the theoretical prediction that certain special ramified shapes can align with the streamlines of a simple shear flow instead of tumbling in the flow. Finally, since the experiments in turbulent flow (section 3) and many applications involve large particles, we developed a slender-body theory that allows for inertial effects in an inner region near the rods. This theory, which is

required when the Reynolds number based on the rod diameter is of order one, is described in section 6. The work in sections 1-3 are the basis of a paper in preparation for the *Journal of Fluid Mechanics* (Kramel, et al. 2018), section 4 forms the basis of a paper submitted to the *Journal of Fluid Mechanics* (Roy, et al. 2018), and the work in section 5 has been submitted to *Physical Review Fluids* (Borker et al 2018). The work in section 6 will be prepared for publication after the theoretical results for the inertial torque have been validated by comparisons with direct numerical simulations and experiments.

1. Orientation distribution of fibers settling in a turbulent flow for L/η<<1

The response to a turbulent flow of a particle whose length is smaller than the Kolmogorov length scale depends on the fluid velocity gradient that parameterizes the local linear velocity field near the particle. When U/u(η)<<1, this particle's translational motion is similar to that of a fluid particle. Thus, one can consider the particle to experience the fluid velocity gradient evolution in a Lagrangian reference frame. While Guassian random velocity fields have proved useful in describing the influence of the local linear flow field on drop coalescence and particle inertial clustering, these models do not capture the coupling of strain rate and rotation rate arising from vortex line stretching and rotation. To describe the rotation of a particle it is essential to capture the tendency of vorticity to align with the extensional axis of the flow. A velocity gradient model that achieves this was first introduced by Girimaji and Pope (1989). In this model, the velocity gradient tensor (Γ_{ij}) is modeled as a Markovian process that captures the effect of the non-linear inertial terms in the Navier-Stokes equations on the velocity gradient. Direct numerical simulation results show that the pseudo-dissipation, φ, has a log-normal distribution and so it is modeled as the Uhlenbeck-Ornstein (UO) process:

$$d\varphi = \varphi \, dt \left(\frac{\sigma^2}{2\tau} - \frac{\ln \varphi}{\tau}\right) + \sqrt{\frac{2}{\tau}} \sigma \varphi \, dW \tag{1}$$

where σ^2 is the variance of φ, τ is the ratio of the integral and Kolmogorov time scales, dW is the increment of a Wiener process, and times are non-dimensionalized by the Kolmogorov time scale. The velocity gradient (Γ_{ij}) (after correcting a typographical error in [1]) follows:

$$d\Gamma_{ij} = -N_{ij}dt - \Gamma_{ij}\left(\frac{9\sigma^2}{2\tau} + \frac{\ln \varphi}{2\tau} - \frac{\Gamma_{lm}N_{lm}}{\varphi}\right)dt + L_{ij}dt + D_{ijkl}dW_{kl} \tag{2a}$$

$$D_{ijkl} = \sigma\sqrt{\frac{\varphi}{2\tau}}\left(\delta_{ik}\delta_{jl} - \frac{1}{3}\delta_{ij}\delta_{kl}\right) \tag{2b}$$

where

$$N_{ij} = \Gamma_{kj}\Gamma_{ki} - \frac{1}{3}\delta_{ij}\Gamma_{lm}\Gamma_{ml} \tag{2c}$$

arises from the non-linear term in Navier-Stokes equation and L_{ij} is an arbitrary tensor valued function that is determined from the kinematic constraints on the velocity gradient Γ_{ij}. By solving the stochastic differential equation, we obtain velocity gradient that samples an isotropic turbulent flow, using which we are then able to simulate the fiber orientation dynamics. We have compared properties of the velocity gradient tensor obtained using the model to DNS results for moments of the velocity gradient tensor in table 1. In the table, *s* and *r* correspond to the symmetric and anti-symmetric parts of the velocity gradient **Γ**. These statistics include the correlation of the strain rate and vorticity, which is of critical

importance for Lagrangian models to successfully capture particle orientational dynamics. As can be from the table, our results match the DNS results reasonably well.

Table 1 Velocity gradient statistics obtained from the stochastic model are compared to the DNS results of Yeung and Pope (1989).

Means of	DNS	Lagrangian Model
$tr\ \boldsymbol{ss}$	0.498	0.560
$-tr\ \boldsymbol{rr}$	0.511	0.488
$tr\ \boldsymbol{sss}$	-0.113	-0.146
$tr\ \boldsymbol{srr}$	0.0401	0.0376
$tr\ \boldsymbol{ssrr}$	-0.158	-0.181
$-tr\ \boldsymbol{srr}/(\sqrt{tr\ \boldsymbol{ss}\ tr\ \boldsymbol{rr}})$	0.0737	0.0722
$-tr\ \boldsymbol{srsr}/(tr\ \boldsymbol{ss}\ tr\ \boldsymbol{rr})$	0.263	0.251

The time rate of change of the orientation ($\dot{\boldsymbol{p}}$) of a low Reynolds number, settling, slender fiber is caused by the turbulent velocity gradient ($\dot{\boldsymbol{p}}_{turb}$) and the inertial torque ($\dot{\boldsymbol{p}}_{sed}$). Thus we have:

$$\dot{\boldsymbol{p}} = \dot{\boldsymbol{p}}_{turb} + \dot{\boldsymbol{p}}_{sed} \tag{3}$$

where

$$\dot{\boldsymbol{p}}_{turb} = \boldsymbol{\Gamma}.\boldsymbol{p} - \boldsymbol{p}(\boldsymbol{p}.\boldsymbol{\Gamma}.\boldsymbol{p}) \tag{3a}$$

$$\dot{\boldsymbol{p}}_{sed} = -\frac{5Re_L(\boldsymbol{e_U}.\boldsymbol{p})}{8L\ln 2\kappa}\boldsymbol{U}.(\boldsymbol{I} - \boldsymbol{pp}) \tag{3b}$$

$\boldsymbol{p}$ is the orientation vector, $\boldsymbol{e_U}$ is the unit vector parallel to the fiber settling velocity, Re_L is the Reynolds number based on the settling velocity and fiber length, and κ is the particle aspect ratio. The rotation due to the turbulent shearing motion is described by Jeffery (1922) rotation in a local linear flow, while the rotation due to the inertial torque is derived from the slender-body theory of Khayat and Cox (1989). We can define a dimensionless parameter, called the settling factor S_F, which measures the relative magnitude of the rotation due to the sedimentation torque and the turbulent velocity gradient:

$$S_F = \frac{5Re_LU}{8L\Gamma_\eta \ln 2\kappa} = \frac{5}{8\ln(2\kappa)}\left(\frac{U}{u(\eta)}\right)^2 \tag{4}$$

where Γ_η is the Kolmogorov shear rate.

The simplest measure of the orientation distribution of settling axisymmetric particles is the variance $<p_3^2>$ of the gravity-component of the orientation of the particle's axis of symmetry. The variance obtained by averaging over many fibers that had experienced the Lagrangian turbulent velocity gradient model long enough to reach a statistical steady state is presented as the circles in Figure 3. For small settling factors, $S_F \ll 1$, the particle orientation variance is

$$<p_3^2> = \frac{1}{3} - 0.65S_F \tag{5}$$

where the first term on the right-hand side of (5) corresponds to the isotropic distribution of fibers in a turbulent flow in the absence of sedimentation and the second term is a linear perturbation due to weak settling. If we model the influence of turbulence as an effective rotary diffusivity, we would also obtain a linear perturbation for weak settling and comparing the rotary diffusion model to the Lagrangian simulation yield an effective rotary diffusivity of $D_r = 0.017\Gamma_\eta$.

3

In the rapid settling limit ($S_F \gg 1$ or $\frac{U}{u(\eta)} \gg 1$), the particle falls through a "frozen" turbulent field experiencing a strong inertial torque that aligns it horizontally but with weak fluctuations due to multiple turbulent eddies as illustrated in Figure 1.1. The turbulent rotation leads to an isotropic distribution within the horizontal (12)-plane, but there is a small orientational variance in the 3-direction. Because of the small deviation from the horizontal plane, the particle orientation relaxes rapidly and reaches a quasi-steady p_3 due to the balance of the turbulent shear and gravitational torques

$$(\delta_{3j} - p_3 p_j) p_k \Gamma_{jk} = \frac{5 Re_L U \, p_3}{8 \, L \log 2\kappa} \qquad (6)$$

$$p_3 \approx \frac{8L \log 2\kappa}{5 Re_L U} \delta_{i3} \Gamma_{ij} p_j \qquad (7)$$

Using analytical expressions for strain and rotation variances $< s_{ij} s_{mn} >$ and $< r_{ij} r_{mn} >$ in an isotropic turbulent flow we obtain an analytic result for the orientation variance ($< p_3^{\,2} >$) in the rapid settling limit ($S_F \gg 1$)

$$< p_3^{\,2} > = \frac{2}{15} S_F^{-2} \qquad (8)$$

It is interesting to note that the orientational variance in this limit is not described even qualitatively correctly by an effective rotary diffusion model. Such a model would have yielded $< p_3^2 > \sim S_F^{-1}$. The two asymptotes corresponding to the two limiting cases, $S_F \ll 1$ and $S_F \gg 1$, are shown in Figure 1.2.

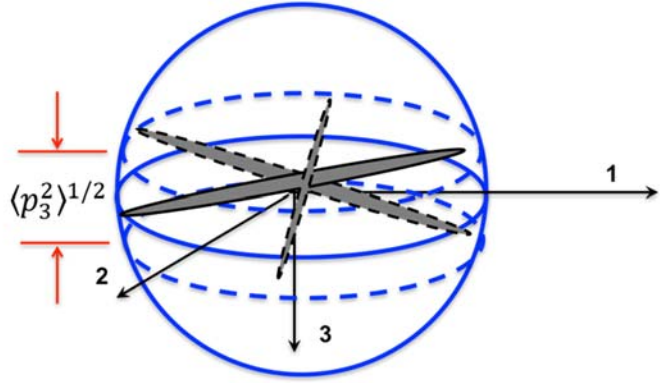Figure 1.1. Particle orientation confined to a thin region near the horizontal plane for $U \gg u(\eta)$

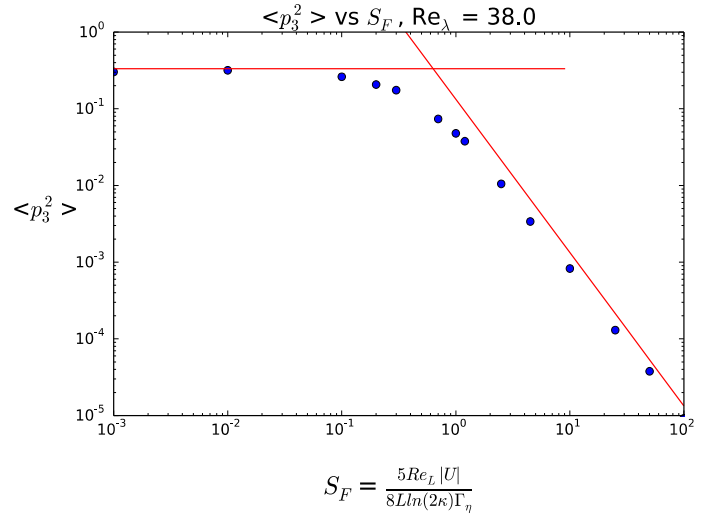$$S_F = \frac{5 Re_L |U|}{8 L ln(2\kappa) \Gamma_\eta}$$

Figure 1.2. Lagrangian simulation of particle orientation as a function of the settling factor.

2. Stochastic model for the orientation of triad particles settling in turbulent flows
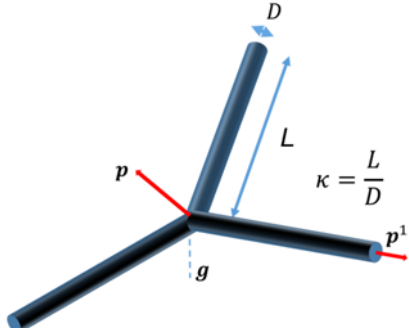

Figure 2.1: Triad with particle and rod orientation

In this section, we extend the stochastic model described in section 1 to the case of a ramified particle and give results for a planar triad. We solved equations of motion for the particle rotation rate, orientation and velocity using a particle model derived from slender-body theory for large rod aspect ratio, $\kappa = \frac{L}{D} \gg 1$, in the case where the Reynolds number based on the rod length, $Re_L = \frac{UL}{\nu}$, is small, but non-zero. As illustrated in figure 2.1, the orientation of the triad can be described in terms of a unit vector, **p**, that is perpendicular to the plane of the particle and unit vectors $\mathbf{p}^n$ parallel to each of the arms. The velocity of the particle is determined by an overall force balance:

$$\sum_{n=1}^{3}\left[\frac{4\pi\mu L}{\ln 2\kappa}\left(\mathbf{I} - \frac{1}{2}\mathbf{p}^n\mathbf{p}^n\right).\mathbf{U}^n - \frac{\pi\Delta\rho D^2 L}{4}\mathbf{g}\right] = \sum_{n=1}^{3}\left[\mathbf{F}^n{}_{drag} + \mathbf{F}^n{}_{gravity}\right] = \mathbf{0}$$

(9)

where $\mathbf{U}^n$ is the velocity of the center of mass of rod n which is determined from the velocity and rotation rate of the particle through a requirement of solid-body motion of the triad. The first term in (1) is the orientation-dependent Stokes flow drag and the second is the gravitational force. The rotation rate of the particle is determined by an overall torque balance:

$$\sum_{n=1}^{3}\left[l\mathbf{p}^n \times \mathbf{F}^n{}_{drag} + \frac{5\pi\rho L^3}{24(\ln 2\kappa)^2}(\mathbf{U}^n.\mathbf{p}^n)(\mathbf{U}^n \times \mathbf{p}^n) - \frac{\pi\mu L^3}{3\ln 2\kappa}(\mathbf{I} - \mathbf{p}^n\mathbf{p}^n).\mathbf{\Omega} - \frac{\pi\mu L^3}{3\ln 2\kappa}((\mathbf{E} \ .\mathbf{p}^n) \times \mathbf{p}^n\right] = \mathbf{0}$$

(10)

The first term in (2) is the torque about the triad center of mass due to the drag on the rods, where $l = L/2$ is the rod half-length and the distance between the particle and rod center of mass. The second term is the inertial torque due to settling which favors horizontal orientations. This is the only term in the model that includes fluid inertial effects on the particle scale and it is based on the low Re_L limit of the inertial torque derived using slender-body theory by Khayat and Cox (1989). Since particles settling in a quiescent fluid at zero Reynolds number do not rotate, the inclusion of this term is necessary to capture the leading order rotation at low Reynolds number. The final two terms in (2) describe the particle rotation due to the turbulence. In the third term, $\mathbf{\Omega}$ is the relative rotation of the particle and the fluid and in the fourth term **E** is the strain rate tensor of the turbulent flow.

The model equations (9) and (10) were solved for a triad experiencing the Lagrangian turbulent velocity gradient predicted by the stochastic model of Girimaji and Pope (1990). The dependence of particle orientation on turbulence intensity is illustrated in figure 2.2, which is a plot of the order parameter $< \cos^2\theta >$ versus S_F. Here θ is the angle between the normal vector to the particle **p** and the direction of gravity. At small S_F, turbulence leads to an isotropic distribution corresponding to $< \cos^2\theta >= 1/3$ and at large S_F the particles become horizontal so that $< \cos^2\theta >= 1$.

The black points representing $0.5(1 - \langle cos^2\theta \rangle)$ allow one to see the deviation from horizontal alignment. The probability distribution functions of particle orientation plotted in figure 2.3 show a transition from nearly isotropic distributions for $S_F = 0.1$ to sharply peaked distributions for $S_F = 2$.
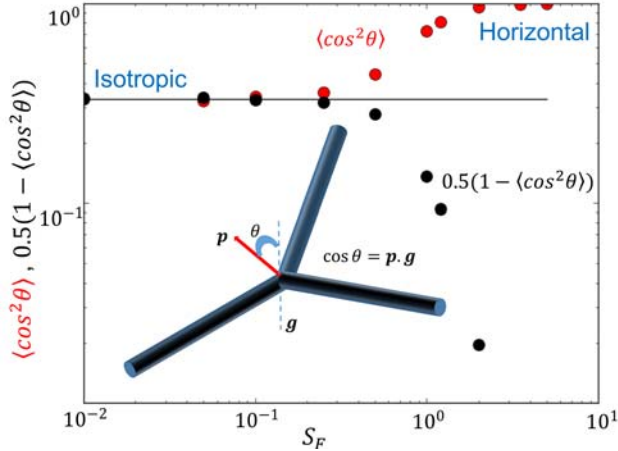

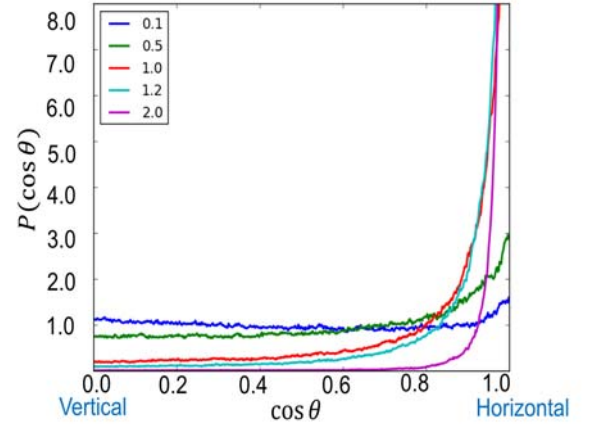Figure 2.2: Order parameter as a function of settling parameter.

Figure 2.3: Probability distribution function of particle orientation at different values of the settling parameter (inset).

3. Measurements in the vertical water tunnel

During the first year of the grant, we constructed a vertical water tunnel for measurements of alignment and dispersal of non-spherical particles in a flow with controlled turbulence intensity. This past year we have performed a set of experiments using 3D printed triad particles and fibers in this flow. A schematic and image of the facility are show in Figure 3.1. Four video cameras are configured to view a central region of roughly $(10 \text{ cm})^3$, and LED backlighting allows bright field imaging.
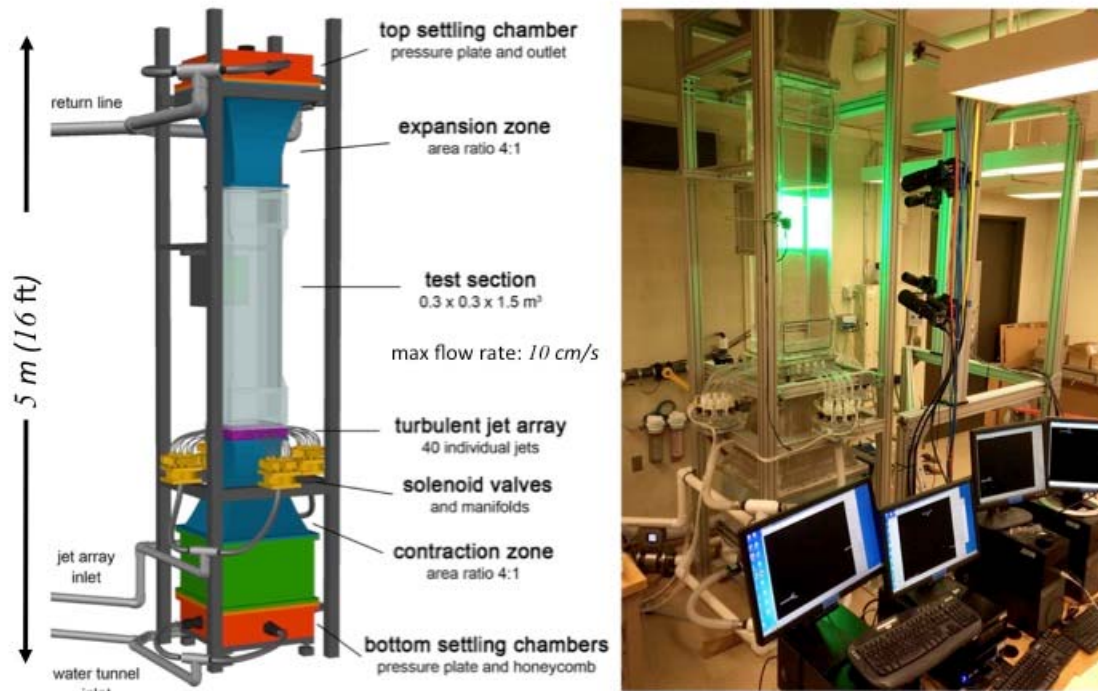
Figure 3.1: Vertical Water Tunnel. A grid containing an array of solenoid controlled jets controls the turbulence intensity.   The mean velocity can be adjusted to balance the mean sedimentation velocity.

To provide a foundation for the experiments in turbulent flow, we measured the vertical (sedimentation) velocity and horizontal (dispersal) velocity of triads and fibers in quiescent fluid flow, shown in Figure 3.2. When normalized by the aligned velocity, the data is fairly well represented by the model in section 2 shown with dashed lines. However, the actual vertical velocity of the particles differs substantially from the model due to the fact that the experiments have Re_D of 10 for small triads and 35 for large triads. One conclusion of our work so far is that the low Re_D and Re_L model in section 2 accounts quite well for sedimenting particle motion in turbulence if it adjusted to match empirical values for the aligned sedimentation velocity.
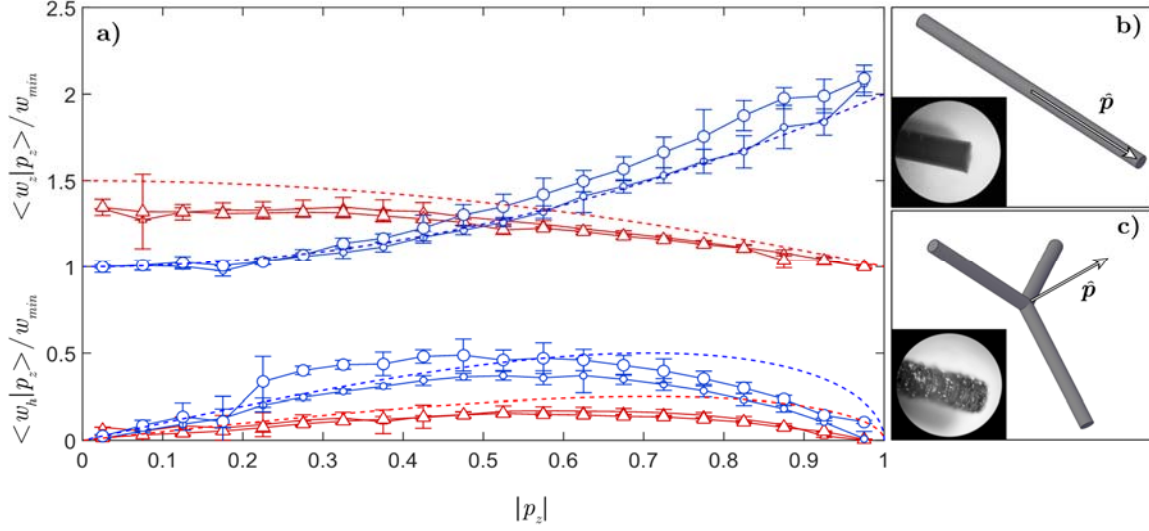
Figure 3.2: Vertical particles velocity (top blue for fibers and red for triads) and horizontal particle velocity (bottom blue for triads and red for fibers) as a function of orientation in quiescent fluid. All velocities are normalized by vertical velocity of

In Figure 3.3, we show the dependence of particle alignment on the turbulence intensity in the experiments. When plotted as a function of the settling factor, S_F, the experiments show good collapse with the simulations indicating that we have correctly identified the non-dimensional parameter that controls particle alignment in turbulent sedimentation.
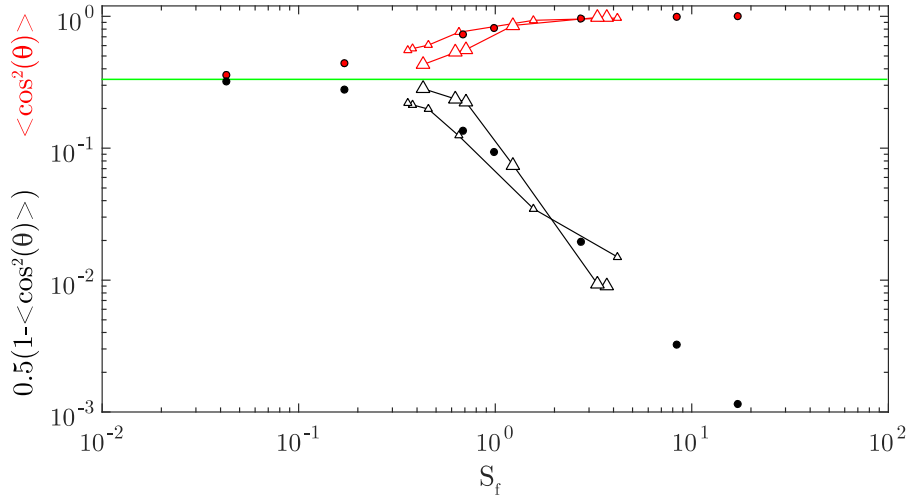

Figure 3.3: Alignment of triads as a function of settling factor, S_f, in experiments with varying turbulence intensity. Large triangles are large triads and small triangles are small triads. Solid symbols are the simulations shown in Figure 5. Red and black data show the same data with black plotted to show the deviation from horizontal alignment.
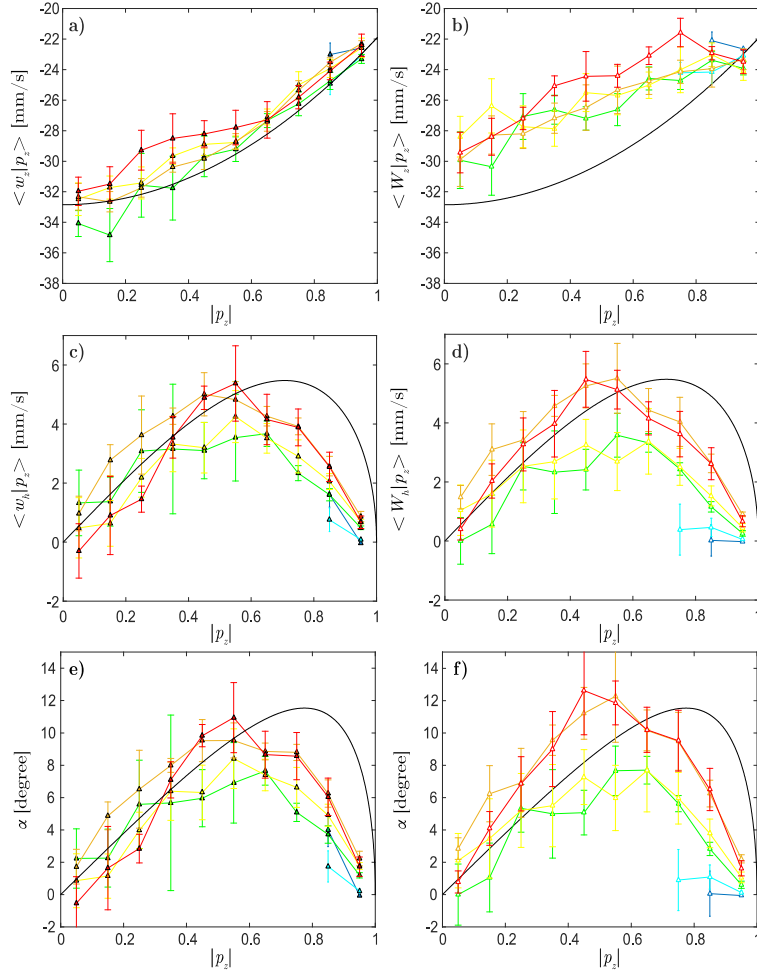
Figure 3.4: Mean vertical (a,b) and horizontal (c,d) velocity of sedimenting triads as a function of orientation. (a, c) show the mean velocity with respect to the local fluid velocity. (b,d) show the mean velocity with respect to the mean fluid flow. (e) shows the angle between the particle velocity and the local fluid velocity while (f) shows the angle with respect to the mean fluid velocity.

Figure 3.4 shows the mean particle velocity in turbulent flow with respect to the local fluid velocity and the mean fluid velocity. We measure tracer particles in the vicinity of the particle which allow us to define an average velocity of all tracers found within one particle diameter of the particle. Access to both this coarse-grained fluid velocity and the particle motion allows detailed analysis of the causes of the measured particle velocity. One particular conclusion from this data is from the difference between figures 3.4(a) and 3.4(b). The simple ramified particle model from section 3 shown in the solid line is in much better agreement when compared with the local fluid velocity than with the mean velocity. This indicates that particles are preferentially sampling upwelling regions causing their vertical velocities to be smaller than predicted if only the mean flow was considered.

9

4. Inertial torques and a symmetry breaking transition to oblique sedimentation of rodlike particles

The theories described in sections 1 and 2 for ramified particle orientation in turbulent flow build upon the slender-body theory of Khayat and Cox (1989) which accounts for fluid inertia by solving the Oseen equation in an outer region (separations on order of the particle length) while neglecting inertia in the inner region (within a rod diameter from the particle surface). Since there are few measurements available to validate this important theory, we undertook observations of the settling of symmetric and asymmetric fibers in a quiescent fluid choosing particles that conform as closely as possible to the asymptotic regime for which the theory is applicable. These correspond to small Reynolds number based on the fiber diameter $Re_D = \frac{UD}{\nu} \ll 1$, moderate Reynolds number based on the fiber length $Re_L = \frac{UL}{\nu} \ll \ln \kappa$, and high aspect ratio $\kappa = \frac{L}{D} \gg 1$. We chose $Re_D \approx 0.15 - 0.17$ for which the effects of inertia in the inner region are less than 7% (based on the theory in section 6). Two symmetric fibers of different length then yielded $\kappa = 20$; $Re_L = 1.6$ and $\kappa = 100$; $Re_L = 8.6$. The sedimentation velocity and inertial rotation rate were measured by dropping particles with initial oblique orientations. Figure 4.1 shows the inertial torque (symbols) compared with the theoretical predictions (dotted line) obtained by assuming a balance between the inertial torque due to sedimentation and a viscous quasi-steady resistance to rotation. The agreement is quite good even for the larger particles for which the condition $Re_L \ll \ln \kappa$ is not strictly met.
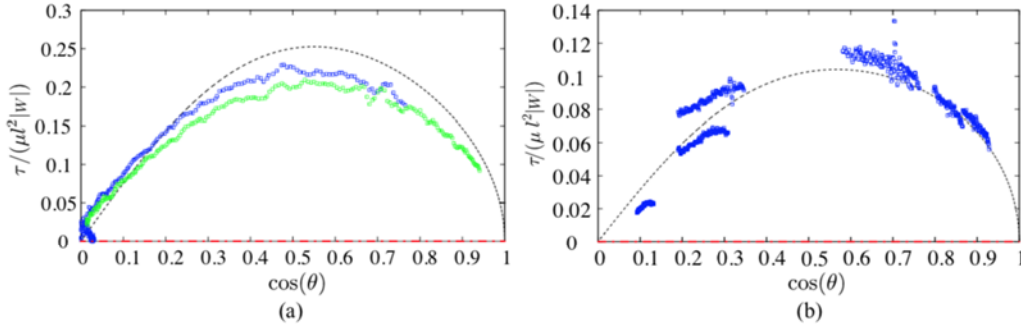

Figure 4.1: Inertial torque on a symmetric fiber settling in a quiescent fluid as a function of angle q of the fiber axis relative to gravity for (a) $\kappa = 20$; $Re_L = 1.6$ and (b) $\kappa = 100$; $Re_L = 8.6$. Symbols are experimental measurements and dotted line is the theory of Khayat and Cox (1989).

A measurement of the inertial torque without the need to invoke a quasi-steady viscous resistance to rotation can be obtained if a fiber achieves a steady oblique orientation due to the balance of the inertial torque with a gravitational torque. To investigate this possibility, we derived the fixed orientations and their stability for two types of asymmetric fibers: a particle P1 which has a constant diameter but a difference in mass density with axial position and a particle P2 which has a step change in diameter with axial position. Particle P1 was realized experimentally by injecting bubbles into the glue in the interior of a glass capillary. Figure 4.2 shows that the orientations of both types of particle undergo a

supercritical pitchfork bifurcation with increasing Archimedes number $\mathrm{Ar} = \frac{\Delta\rho g V_p \ln\kappa}{2\pi\mu\nu}$, where $\Delta\rho$ is the density difference between the particle and fluid and V_p is the particle volume. The Archimedes is approximately $\mathrm{Re}_L/2$ at small Ar. At small Archimedes numbers, the fiber settles in a vertical orientation. This fixed point for P1 becomes unstable above a critical Archimedes number $\mathrm{Ar_{cr}} = 3.45$ because the inertial torque at small deviations from $\theta = 0$ overcomes the gravitational torque. Above this Archimedes number the orientation is oblique. For particle P2, the critical Archimedes number is smaller, $\mathrm{Ar_{cr}} = 0.44$, because there is a viscous torque that rotates the thicker part of the fiber downstream and this aids the inertial torque in overcoming the gravitational torque.
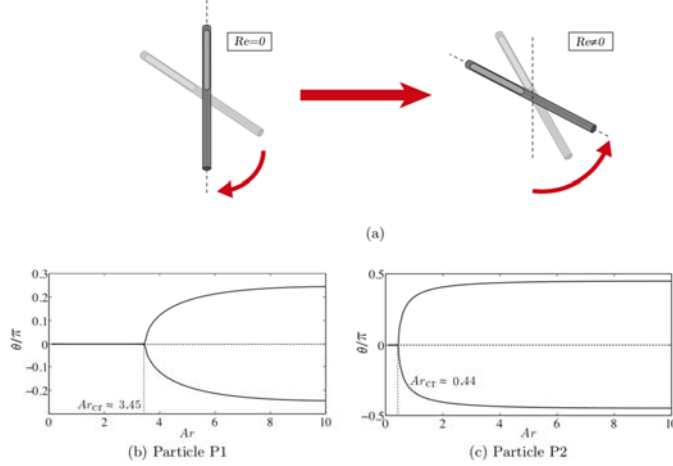

(a)

(b) Particle P1   (c) Particle P2

Figure 4.2: The orientation θ of an asymmetric fiber with respect to vertical for $\kappa = 39.7$ and $\delta = 0.015$, where $\delta = R_{\mathrm{com}}/l$ is the ratio of the distance of the center of mass of the particle from its geometric center and the fiber half-length. Solid and dotted lines indicate stable and unstable fixed points, respectively.

At a fixed Archimedes number, the orientation transitions from vertical to oblique below a critical value of the asymmetry parameter $\delta = R_{\mathrm{com}}/l$, where R_{com} is the distance of the center of mass from the geometric center of the particle. This transition is seen in the experimental measurements (symbols) in Figure 4.3 where it is compared with theoretical predictions for two Archimedes numbers that span the range of Ar in the experiments. The oblique orientations are in good agreement with the theory, while the transition occurs at a slightly higher δ than the theoretical prediction. This may be due to the fact that the Khayat and Cox (1989) theory slightly underpredicts the inertial torque at moderate Re_L.

Symmetric non-spherical particles settling in a turbulent environment undergo significant horizontal dispersive motion due to turbulence-induced orientation changes and the orientation-dependent
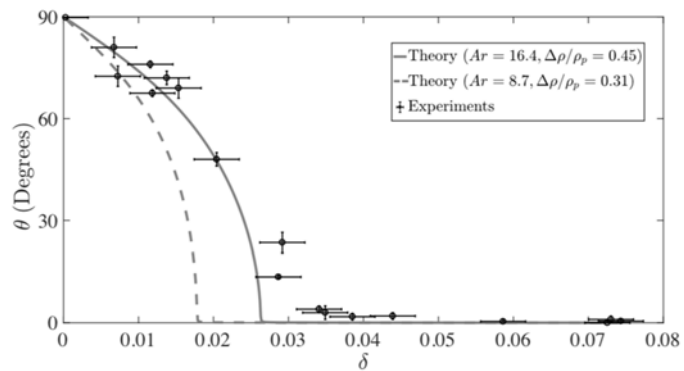

Figure 4.3: Equilibrium settling orientation for $\kappa = 40$ particles as a function of the asymmetry parameter δ.
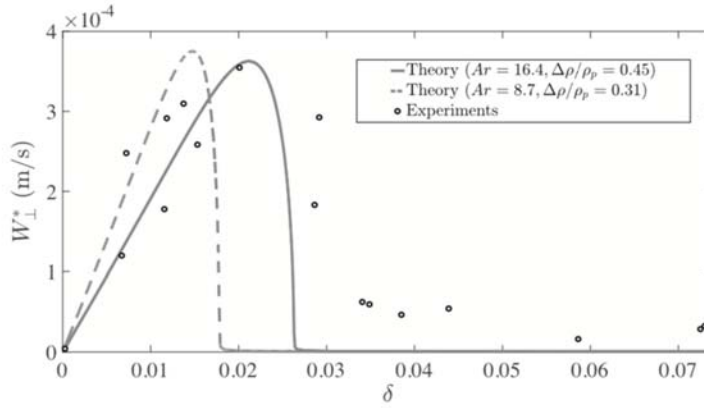
Figure 4.4: Horizontal component of settling velocity of asymmetric $\kappa = 40$ particles as a function of the asymmetry parameter δ.

settling velocity as illustrated in section 3. However, in a low turbulence environment, symmetric particles would take on a broadside orientation and settle vertically. Strongly asymmetric particles will take on a bottom-heavy vertical orientation in a quiescent fluid and again settle vertically. However, fibers with finite asymmetry that is below a critical value, δ_{cr}, having oblique orientations, settle with a horizontal component to their velocity. This behavior is seen in Figure 4.4 in both experimental measurements and theoretical predictions. Thus, particles with $0 < \delta < \delta_{cr}$, could be consider self-dispersing.

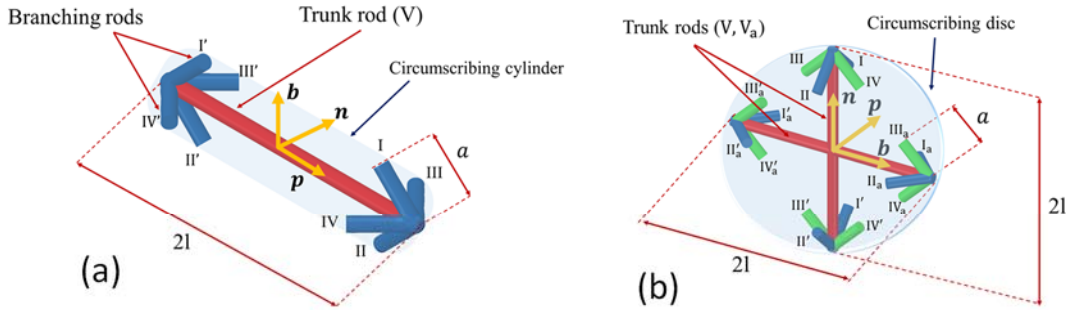## 5. Controlling particle rotation in simple shear flow using ramification

Figure 5.1: Ramified particles that resist rotation in a laminar simple shear flow. (a) A ramified cylinder; (b) a ramified planar cross.

While the primary focus of this project has been on the orientation of non-spherical particles settling in turbulent flow, we have also discovered an interesting way in which ramified shapes can be used to tune the rotation of a particle in a laminar shearing flow at low particle Reynolds number. Most axisymmetric particle tumble continuously in a simple shear flow at low Reynolds number following a motion first described by Jeffrey (1922). However, we have shown that certain ramified particles can cease rotating and align nearly parallel to the streamlines of the flow. The aligning particle shapes are illustrated in Figure 15. A linear, aligning shape consists of a trunk rod with 4 symmetrically placed branching rods in an arrow-like configuration at each end of the trunk rod. A planar aligning shape can be obtained by similar ramification of a planar cross particle as illustrated in figure 5.1b. The mechanism leading to alignment is illustrated in Figure 16. Being aligned
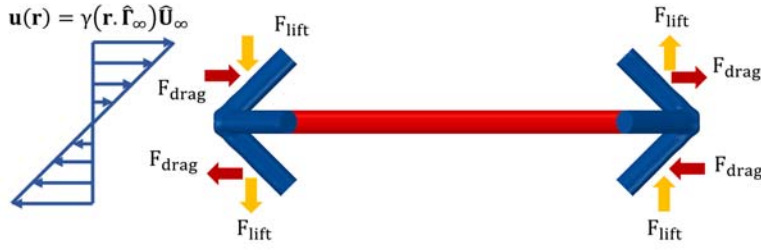
Figure 5.2: Mechanism leading to flow alignment. The lift forces acting on the branching rods create a counter-vorticity torque that can balance the torque due to drag and stabilize a fixed particle orientation.

at an oblique angle to the imposed flow, the branching rods experience both a lift and drag force due to the orientation dependence of the viscous resistivity of the rodlike shape. While the drag forces create a torque on the particle that favors tumbling in the flow, the lift forces induce a counter-vorticity torque on the particle. With a suitable choice of the length and angle of the branching rods these torques can balance to create a stable stationary orientation. To obtain quantitative predictions, we performed slender-body calculations on these ramified particles. Figure 17 shows the period of rotation in a simple shear flow predicted for a ramified fiber as a function of the angle δ between the trunk and branching rods. The period of rotation is always greater than that of a circumscribing cylinder. In the range $0.706 < \delta/\pi < 0.776$, the period diverges and the particle remains permanently aligned.
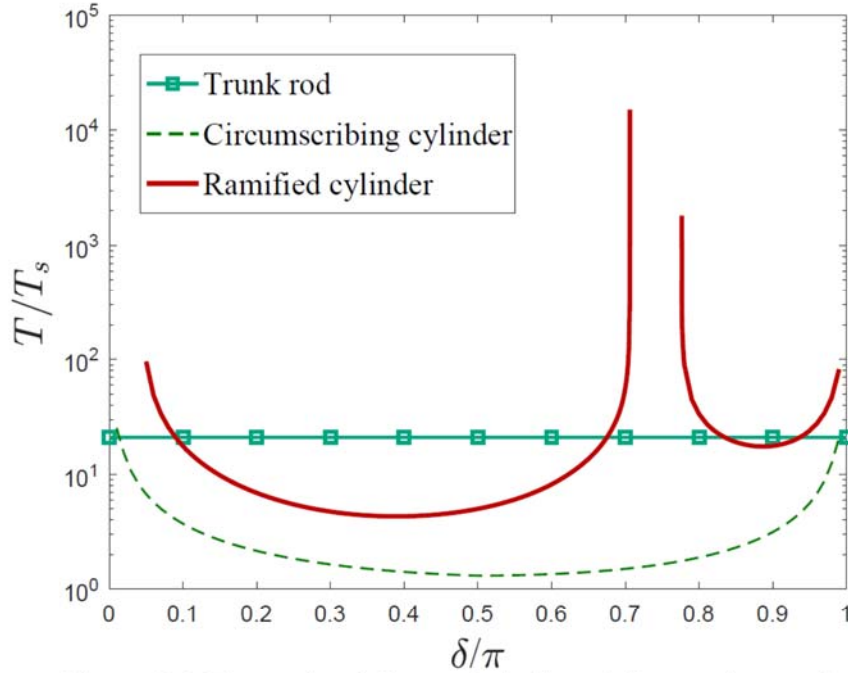

Figure 5.3: The ratio of the period of particle rotation to that of a spherical particle is plotted as a function of the branching angle. Calculations are performed for an aspect ratio 120 trunk rod and the aspect ratio of the branching rods is 24. The period of the ramified particle is compared with that of the trunk rod and of a circumscribing cylinder.

13

6. Slender-body theory for finite Reynolds number based on particle diameter

Because of the high aspect ratio $\kappa = \frac{L}{D} \gg 1$ of the rods making up the ramified particles under study, one can define two distinct particle Reynolds numbers, $Re_L = \frac{UL}{\nu}$, which characterizes the importance of inertia on scales of the particle length, and $Re_D = \frac{UD}{\nu}$, which quantifies inertial effects within distances on the order of a particle diameter from the rod axis. The triad theory described in section 1 is based on slender-body theory results obtained from a perturbation analysis that captures the first effects of inertia for $Re_L \ll 1$. Previous studies (Khayat and Cox 1989; Shin *et al* 2006, Shin *et al* 2009) that have incorporated fluid inertia in slender-body theory (SBT) have considered only inertial effects over the scale of the particle length and therefore have corresponded to $Re_D = 0$. On the other hand the particles used in the experiments in section 2 as well as many practical applications have values of Re_D on the order of 0.1 to 10 where inertial effects play a role in the regions near the rod axis. Thus, we are developing the first slender-body theory for moderate Re_D.

Let us consider a slender body settling under gravity with velocity U (see figure 6.1). We consider the body to have a straight center-line and circular cross-section in the present analysis. In absence of fluid inertia the force acting on the body can be obtained from slender body theory (SBT) (Batchelor 1970), an asymptotic technique valid in the limit of large aspect ratio $\kappa = L/D \gg 1$. This standard SBT is based on a quasi-two-dimensional solution of the Stokes equations in an inner region near the rod and a Green's function treatment of the Stokes flow velocity due to a line of forces in the outer region as illustrated in figure 5b. From SBT we have at leading order,

$$\frac{\boldsymbol{F}}{2\pi\mu UL} = \frac{1}{\log 2\kappa}\left(\mathbf{I} - \frac{1}{2}\mathbf{pp}\right) \cdot \mathbf{U} \tag{11}$$

where μ is the fluid viscosity, $\boldsymbol{p}$ the unit vector indicating the orientation of fiber axis $\boldsymbol{U}$ is the fiber velocity.
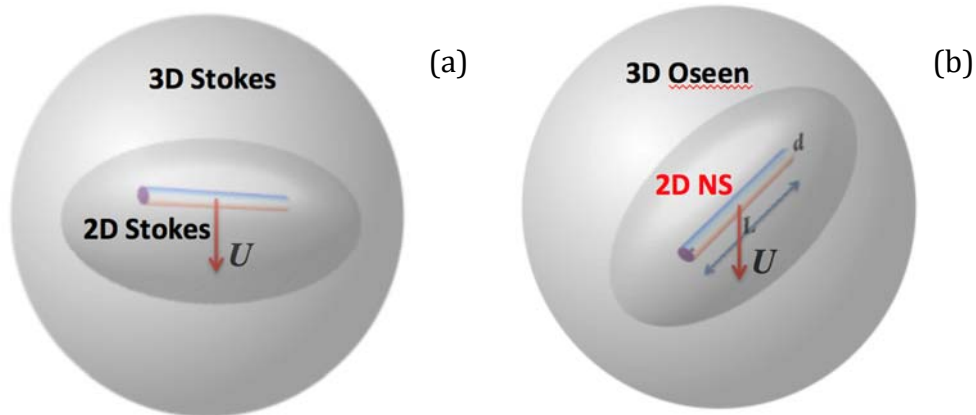

Figure6.1: (a) $Re_D, Re_L = 0$ Slender Body Theory (Batchelor 1970)
(b) Present work - $Re_D, Re_L \neq 0$ Slender Body Theory

The finite Re_D slender-body theory is based on a quasi-two-dimensional solution of the Navier-Stokes equations in the inner region and a three-dimensional

solution of the Oseen approximation to the Navier-Stokes equations in the outer region as illustrated in figure 9b. The use of the linearized Navier-Stokes equation in the outer region is justified based on the observation that the fluid velocity disturbance produced by the rod decays and becomes smaller than U at separations from the rod greater than D.

To develop the inertial slender body theory, we consider the linearized version of the steady state Navier Stokes equation, the Oseen's equation, forced by fiber force per unit length $\boldsymbol{f}(s\boldsymbol{p})$

$$-Re_l \boldsymbol{U}.\nabla \boldsymbol{u} - \nabla^2 \boldsymbol{u} + \nabla p = \int_{-1}^{1} ds \boldsymbol{f}(s\boldsymbol{p})\delta(\boldsymbol{x} - s\boldsymbol{p}) \qquad (12)$$

where

$$f_i(s\boldsymbol{p}) = \frac{4\pi}{\log 2\kappa}\left[A\left(\delta_{ij} - p_i p_j\right) + \frac{B}{2}p_i p_j\right]\left(U_j - u_j^I(s\boldsymbol{p})\right) \qquad (13)$$

$u_i = u_i^S + u_i^I$, u_i^S is the singular Stokes disturbance field, u_i^I the inertial contribution (Shin, Koch and Subramanian 2009), $Re_l = Ul/\nu$ is the Reynolds number based on the fiber half-length $l = L/2$, and s is the position along the rod axis non-dimensionalized by l. A and B are determined by matching the 3D Oseen calculation with the solution of 2D Navier-Stokes equation (see figure 9b).

Khayat and Cox (1989) solved the Oseen equations (12) and (13) using a regular perturbation expansion valid when $\frac{Re_l}{\ln(\kappa)} \ll 1$. Shin $et\ al$ (2006,2009) solved (12) and (13) using Fourier transforms without restriction on the range of Re_l. This distinction is important because the matching required for the finite Re_D theory requires that the outer solution approach a two-dimensional solution of Oseen's equations as $Re_l \rightarrow \infty$. Shin $et\ al$'s method satisfies this criterion while Khayat and Cox' does not. While Shin $et\ al$ performed the Fourier inversion integrals numerically, we have been able to obtain analytical forms of these integrals. The analytical results are valuable because the numerical integration becomes exceedingly stiff at the $O(100)$ value of Re_l applicable to our experimental study.

Matching of the inner and outer solutions, leads to expressions for the coefficients of the transverse and longitudinal drag coefficients in the finite Re_D SBT in terms of solutions of Stokes equations, Oseen equations and the full Navier-Stokes equations:

$$A = \left(1 - \frac{C_{D,\text{Batchelor}}}{C_{D,\text{Lamb}}} + \frac{C_{D,\text{Batchelor}}}{C_{D,\text{Keller}}}\right)^{-1} \qquad (14)$$

$$B = \left(1 - \frac{C_{D,\text{Batchelor}}}{C_{D,\text{Tomatika}}} + \frac{C_{D,\text{Batchelor}}}{C_{D,\text{Oblique2D}}}\right)^{-1} \qquad (15)$$

where $C_{D,\text{Batchelor}}$, $C_{D,\text{Lamb}}$, $C_{D,\text{Keller}}$, $C_{D,\text{Tomatika}}$ & $C_{D,\text{Oblique2D}}$ are the drag coefficients ($F/(\rho U^2 Dl)$) from the following theories respectively - finite aspect ratio Stokes (Batchelor 1970), 2D Oseen (small $Re_D \ll 1$) (Lamb 1932), 2D Navier-Stokes ($Re_D \sim O(1)$) (Keller and Ward 1996), Oblique infinite cylinder (small $Re_D \ll 1$) (Tomotika and Aoi 1953) and Oblique infinite cylinder Navier-Stokes (to be determined numerically). The oblique infinite cylinder calculations involve a solution of the two-dimensional flow transverse to the cylinder equivalent to that obtained by Keller and Ward but also involve the convection of longitudinal momentum by the transverse fluid velocity. The latter problem is equivalent to a

heat transfer problem with a Prandtl number of 1 and has been solved for the Oseen equations by Tomotika and Aoi (1953) but will need to be determined numerically for the full Navier-Stokes equations as part of our study.

The finite Re_D slender-body theory is a significant improvement over the existing theory of Khayat & Cox. In figure 6.2 we plot comparisons of our theory with experimental results (Tritton 1959 and Jayaweera and Mason 1965), numerical simulations for finite aspect ratio rods (Vakil and Green 2009) and the theory of Khayat and Cox. The black curves and symbols correspond to an aspect ratio of 20 and the blue curves and symbols to an aspect ratio of 100. The solid curves are the
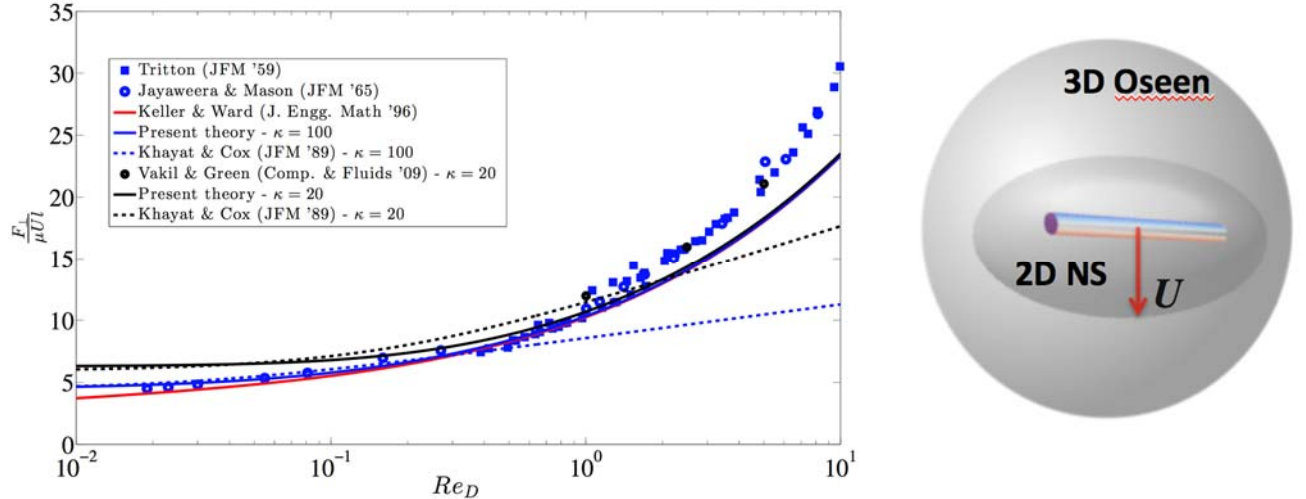

Figure 6.2: Transverse drag on a fiber ($U \perp p$)

present theory and the dashed curves are from Khayat and Cox. It can be seen that the new theory is in good agreement with the theory of Khayat and Cox for small Re_D where the Khayat and Cox theory is applicable. As Re_D increases the results of the new SBT for the two different aspect ratios converge to a single drag coefficient that is independent of aspect ratio when plotted as a function of Re_D and the new SBT results converge with the full Navier-Stokes predictions of Keller and Ward in this case. The new theory is close to the experimental and numerical simulation results whereas Khayat & Cox predicts drag that is almost 3 times smaller.

As a second application of the theory, we consider the drag on a cylinder translating parallel to its axis (figure 6.3). The longitudinal force on the oblique
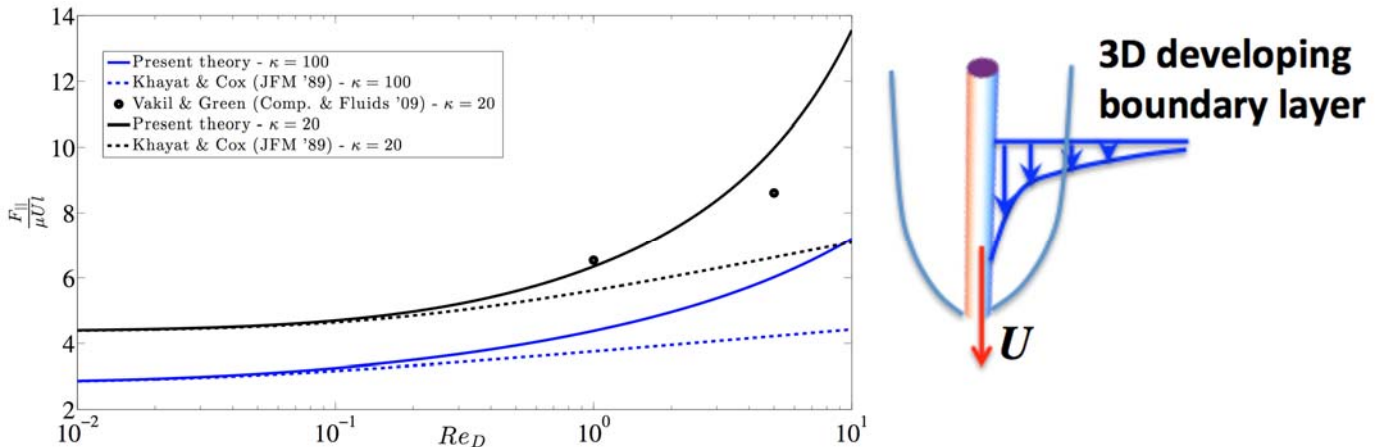

Figure 6.3: Longitudinal drag on a fiber ($U||p$)

16

cylinder using the method indicated in Eq. (8) applies when the angle between the cylinder axis and translational velocity is larger $Re_L^{-1/2}$ so that convection of longitudinal momentum by the transverse velocity field is more important than the longitudinal convection of longitudinal momentum. For a parallel or nearly parallel orientation, one should use the boundary layer formulation of Glauert and Lighthill (1955) on an infinite cylinder as the inner solution. Since we have not yet implemented this inner solution we use a viscous inner solution corresponding to $B = 1$ in figure 7. Despite this limitation, the improved three-dimensional Oseen theory provides a significant improvement in the prediction of the longitudinal drag and is closer to the full numerical simulation by Vakil and Green than is the previous theory of Khayat and Cox.
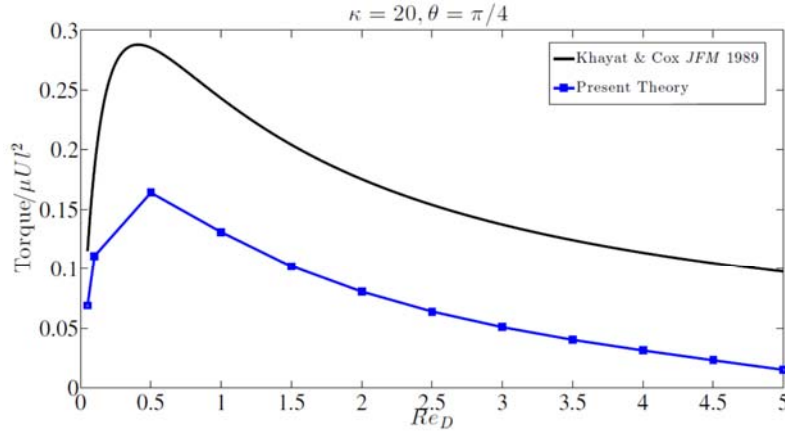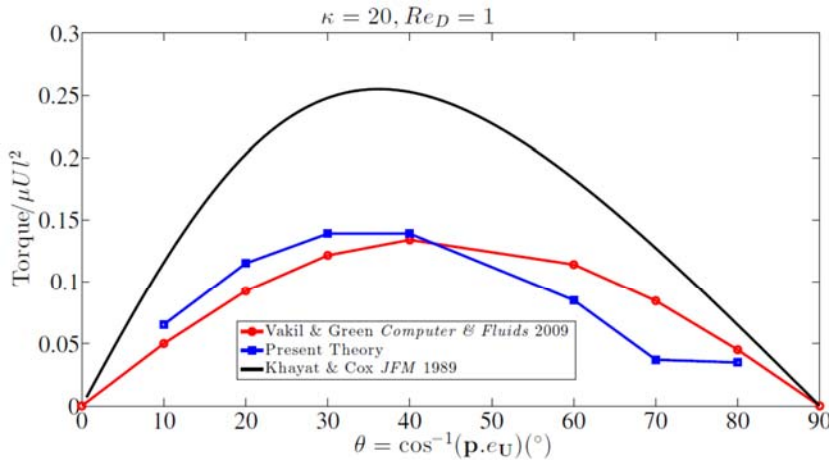

Figure 6.4: Inertial torque on a translating fiber as a function of Re_D for $\kappa=20$ and an angle of $\pi/2$ between the fiber axis and velocity.

Finally, we compute the inertial torque on a translating fiber. Figure 6.4 shows that the inertial torque at finite Re_D is lower than that predicted by the Oseen theory of Khayat and Cox, while both theories predict that the torque passes through a maximum at an intermediate Reynolds number. Figure 6.5 compared the angular dependence of the inertial torque at $Re_D=1$ and $\kappa=20$ computed by the finite Re_D SBT to numerical simulations using a finite volume method. The improved SBT is much closer to the full numerical simulation result than is the theory of Khayat and Cox.

Figure 6.5: Inertial torque as a function of the angle between the fiber Axis and velocity for $\kappa=20$ and $Re_D=1$. The finite Re_D theory (blue) is Compared with numerical simulations (red) and the $Re_D\ll1$ theory (black)

17

References

Batchelor, G. K. "Slender-body theory for particles of arbitrary cross-section in Stokes flow." Journal of Fluid Mechanics **44** (1970): 419-440.

Borker, N.S., Stroock, A.D., and Koch, D.L. 2018 "Controlling particle rotation via ramification." Physical Review Fluids (submitted).

Glauert, M.B. and Lighthill, M.J. "The axisymmetric boundary layer on a long thin cylinder" Proc. R. Soc. Lond. A **230** (1955): 188.

Girimaji, S. S., and S. B. Pope. "A diffusion model for velocity gradients in turbulence." Physics of Fluids A **2** (1990): 242-256.

Jayaweera, K. and Mason, B.J. "The behavior of freely falling cylinders and cones in a viscous fluid" J. Fluid Mech. **22** (1965): 709.

Lamb, H. Hydrodynamics, Cambridge University Press 1932.

Keller, J.B. and Ward, M.J. "Asymptotics beyond all orders for a low Reynolds number flow" J. Engineering Math. **30** (1996): 253.

Khayat, R. E., and R. G. Cox. "Inertia effects on the motion of long slender bodies." Journal of Fluid Mechanics **209** (1989): 435-462.

Kramel, S., Menon, U., Roy, A., Koch, D.L. and Voth, G.A. 2018 "Orientation and sedimentation of ramified particles in turbulence." Journal of Fluid Mechanics (in preparation).

Roy, A., Hamati, R.J., Tierney, L., Koch, D.L., and Voth, G.A. 2018 "Inertial torques and a symmetry breaking orientational transition in the sedimentation of slender fibers." Journal of Fluid Mechanics (submitted).

Shin, M., Koch, D.L. and Subramanian, G. "A pseudospectral method to evaluate the fluid velocity produced by an array of translating slender fibers." Physics of Fluids **18** (2006): 063301.

Shin, M., Koch, D.L. and Subramanian, G. "Structure and dynamics of dilute suspensions of finite-Reynolds-number settling fibers." Physics of Fluids **21** (2009): 123304.

Tomotika, S., Aoi, T. and Yosinobu, H. "On the forces acting on a circular cylinder set obliquely in a uniform stream at low values of Reynolds number" Proc. R. Soc. Lond. A **219** (1953); 233.

Tritton, D.J. "Experiments on the flow past a circular cylinder at low Reynolds numbers" J. Fluid Mech. **6** (1959): 547.

Vakil, A. and Green, S.I. "Drag and lift coefficients of inclined finite circular cylinders at moderate Reynolds numbers" Computers and Fluids **38** (2009): 1771. Corrigendum: Computers and Fluids **74** (2013): 126.

Yeung, P. K., and S. B. Pope. "Lagrangian statistics from direct numerical simulations of isotropic turbulence." J. Fluid Mech. **207** (1989): 531-586.